JSCE (Journal of Systems and Computer Engineering)
Vol.7, No.3, July 2026, pp. 255-265
ISSN (online): 2723-1240
DOI : https://doi.org/10.61628/jsce.v7i3.2697

A Deep Learning Framework for Melanocytic Lesion Classification in Whole Slide Images Using CycleGAN-Stain Normalization and ResNet-152

Januardi nasir[1], Yasha Langitta Setiawan[2].
[1]*Nahdlatul Ulama University of West Sumatra, Faculty of Engineering, Information Systems Study Program*
[2]*Padang Panjang Indonesian Institute of the Arts Faculty of Fine Arts and Design Media Production Study Program.*
[1] januardinasir@gmail.com(*)
[2]Yashalangitta@gmail.com

Abstract

Melanoma is one of the deadliest forms of skin cancer and requires accurate pathological diagnosis for effective treatment planning. However, conventional diagnosis of melanocytic lesions remains subjective and is often affected by inter-observer variability, particularly when distinguishing atypical lesions from benign and malignant cases. Furthermore, variations in histopathological staining across medical centers can significantly reduce the generalization performance of deep learning models. This study proposes an intelligent pathological diagnosis framework based on Whole Slide Imaging (WSI), CycleGAN-Stain normalization, and ResNet-152 classification to improve the diagnosis of melanocytic lesions. The dataset consisted of 981 WSI images collected from three medical centers, including 457 malignant, 142 atypical, and 382 benign melanocytic lesions. The proposed framework includes patch generation, stain normalization using CycleGAN-Stain, deep learning-based classification using ResNet-152, and slide-level prediction aggregation. Internal validation was performed using data from Center 1, while external validation utilized datasets from Centers 2 and 3. Experimental results demonstrated that the CycleGAN-Stain method effectively reduced staining variability while preserving histological structures. Compared with conventional stain normalization approaches, the proposed framework achieved superior diagnostic performance. The intelligent pathological diagnosis model obtained an accuracy exceeding 90% on the external test set and achieved the highest Macro-F1 score among all evaluated methods. These findings indicate that the integration of CycleGAN-Stain and ResNet-152 can provide a robust and accurate framework for classifying benign, atypical, and malignant melanocytic lesions from WSI images.

Keywords— Melanocytic Lesions,Whole Slide Imaging (WSI),Deep Learning,CycleGAN-Stain Normalization, ResNet-152

1. Introduction

Skin cancer is one of the most common types of cancer in the world. In Indonesia, the incidence rate of skin cancer is also quite significant. Globocan 2020 data reported around 18,000 cases of skin cancer with a death rate close to 3,000 cases.

Of these, melanoma is indeed rarer than non-melanoma, but has a much higher mortality rate. A study at Dr. Cipto Mangunkusumo Hospital Jakarta in 2014–2017, for example, showed that malignant melanoma accounted for about 5.7% of all skin cancer cases, with a slightly higher incidence in male patients than in women. Similar findings were also reported in several national referral hospitals, that the majority of melanoma patients came at an advanced stage so the prognosis became worse. This condition shows the importance of efforts to improve early detection and develop more accurate and consistent diagnostic methods in Indonesia(Wang et al., 2021).

Melanoma is a very invasive and aggressive type of skin cancer, with a high potential for metastasis to the lymph nodes and bloodstream in any stage. The melanoma mortality rate is reported to be around 80%. Melanoma is classified as a malignant melanocyte lesion, which can also be atypical or benign in shape. In clinical practice, pathological diagnosis is still the gold standard for confirming the presence of melanocyte lesions. Nevertheless, this diagnostic procedure is subjective and often shows inconsistencies in distinguishing benign lesions from malignant lesions, with a degree of variability reaching 45.5% , even higher in the case of atypical lesions(Riesmiyatiningdyah et al., 2022).

Advances in Whole Slide Imaging (WSI) technology in recent years have driven the development of digital pathology. Along with that, artificial intelligence (AI), specifically deep learning (DeepLearning/DL), has shown promising performance in supporting computer-aided pathology diagnosis. However, variations in tissue staining styles between medical centers pose new challenges to the reliability and generalization capabilities of diagnostic models. Based on these conditions, this study utilizes WSI imagery and the DL method to develop an intelligent pathological diagnosis model that is able to distinguish malignant, atypical, and benign leemelanocytes(Priswanto & Santoso, 2022).

Related to previous research, Hekler et al., proposed a ResNetNet-50-based intelligent pathological diagnosis model, which was shown to achieve higher classification accuracy than 11 pathologists (68% vs. 59.2%). Furthermore, Brinker et al. developed a ResNeXt50-based model as an improvement over ResNet-50, and the results showed a comparable proportion of 18 senior pathologists (88.0% vs. 90.3%). Li et al. then designed a novel convolutional neural network architecture, which resulted in the highest accuracy so far (92.0%) in the classification of benign and malignant melanocyte lesions(Rani et al., 2023).

These findings reinforce the evidence that the DL approach can provide accurate pathological diagnosis results for both benign and malignant melanocyte lesions(Bian et al., 2025)(Icanervilia et al., 2023).

However, there are several limitations that are still the main problem. First, the model's ability to distinguish atypical melanocyte lesions has not been widely studied. In fact, clinically patients with atypical melanocyte lesions require a different surgical treatment plan compared to patients with benign or malignant lesions. However, the similarity in histological patterns and biological characteristics between atypical lesions and benign and malignant lesions often leads to diagnostic confusion. Therefore, accurate differentiation of atypical melanocyte lesions has a very important clinical value(Priswanto & Santoso, 2022)(Smoczek, 2013).

Second, there is still limited research related to the handling of coloring variations in multi-flashlight WSI. Most previous studies used data from patients diagnosed in the same year and from a single medical center, so the consistency of staining was relatively good. This has an impact on the limitation of model generalization, making it less effective when applied to WSI with high coloring variations. Efforts to normalize DL-based staining have indeed been proposed, for example by using self-coded convolutional neural networks to standardize the coloring styles of various medical centers. However, the method still requires paired data, which is an image of the same network slide scanned by two different scanners. This need is difficult to meet in real clinical practice, so its application becomes limited(Amrutkar et al., 2008)(Nunez & Barrios, 2023).

In summary, the current research on computer-aided pathological diagnosis of WSI-based melanocyte lesions still faces two main problems. First, there is a lack of research that specifically addresses the differentiation of atypical melanocyte lesions. Second, the limitations of the model in addressing staining variation across medical centers, which reduces the generalization capabilities of the system(Sun et al., 2024)(Yang et al., 2022). Therefore, further research is needed to develop more robust, accurate, and applicable intelligent pathological diagnosis models in real clinical practice, including in Indonesia, where the burden of skin cancer cases, especially melanoma, remains a serious public health problem(Ashokan, 2024)(Lorandi et al., nd).

.

2. Method

2.1 Method Architecture

This study proposes an intelligent pathological diagnosis method for melanocytic lesions based on DL, which consists of four modules (Fig. 1): Spot generation, staining normalization, DL prediction, and prediction result aggregation.

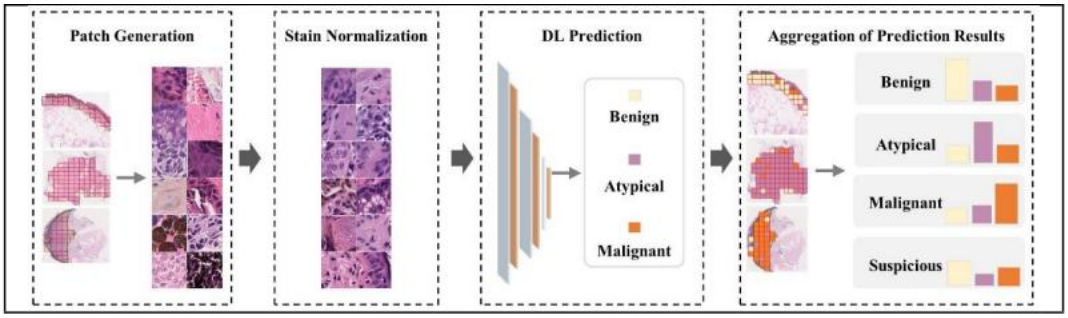

Figure 1.*Our framework for intelligent pathological diagnosis methods for melanocytic lesions*

2.2 Patch Creation

Limited by hardware computing resources, DL methods cannot directly handle WSIs containing hundreds of millions of pixels. Therefore, in this study, the annotated WSI information was used to extract image patches (224 × 224 pixels) from the annotated regions in a non-overlapping manner, and image patches with less than 60% effective network were discarded. To ensure the balance of the image patch dataset for training an intelligent pathological diagnosis model, this study randomly extracted image patches from the WSIs of malignant, atypical, and benign melanocytic lesions in the training set with a ratio of 1:3:1. Finally, 20,000 samples were randomly drawn for each category to balance the number of image patches for the three categories of melanocytic lesions.

2.3 Stain Normalization

Inspired by the work of Shaban et al. , this study frames the normalization of pathological image colorization as a color style transfer problem and designs a colorization normalization method, CycleGAN-Stain, based on CycleGAN. This method uses a K-means color clustering strategy to generate two sets of pathological images: Domain A (with diverse colorization styles) and Domain B (with relatively uniform colorization styles). Then, CycleGAN is used

to convert the image styles of Domain A to Domain B. Due to the long sampling period (from 2001 to 2018) for slides from Center 1, there are significant differences in colorization styles across WSIs. A subset of image patches from Center 1 was randomly selected to form Domain A, which is characterized by distinct colorization styles. K-means clustering was then applied to further analyze these colorization style differences. K-means colorization style clustering was used to define Domain B with relatively consistent colorization styles. The specific steps are as follows.First, the stain concentration matrix $A = [a]i$ of each image patch in Domain A is calculated, where $i = 3$ denotes three channels R , G, and B ; and $j = 2$ denotes two stains H and E . That is, ai is the concentration of stain j in channel i. This study calculates the average value of three channels of each stain for visualization and maps the image patches into two-dimensional features (aH, aE) (Fig. 2). Then, these features are divided into five different stain styles using the K-means clustering method (k = 5). We assign the image patches corresponding to the feature class with the most concentrated styles as the Domain B dataset.

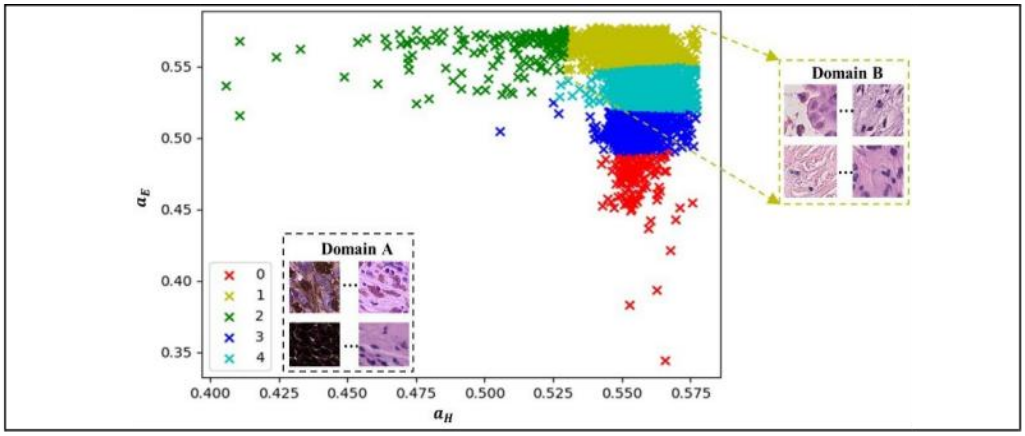

Figure 2.*K-means coloring style clustering visualization*

The CycleGAN-Stain architecture is shown in Figure 3. It consists of two cyclic networks: Domain A → Domain B (forward cycle, solid green arrow) and Domain B → Domain A (backward cycle, solid red arrow). In the forward loop, the cycle consistency loss between aa and a is calculated as follows:

$$L_{cycle}(G_A, G_B, A) = \mathbb{E}[\|a - G_B(G_A(a))\|_1] \quad (1)$$

The discriminator $DDBB$ is used to determine the truth of the real image b and the generated image b in Domain B, and the adversarial loss in the forward cycle is defined as follows:

$$L_{adv}(G_A, G_B, A, B) = \mathbb{E}[logD_B(b)] + \mathbb{E}\left[log\left(1 - D_B(G_A(a))\right)\right] \quad (2)$$

The cycle consistency loss function and the adversarial loss function in the reverse cycle are calculated in a similar manner to the forward cycle, and the overall loss function is the sum of the four losses. The generator and discriminator use a ResNet and a 70x70 PatchGAN network, respectively.

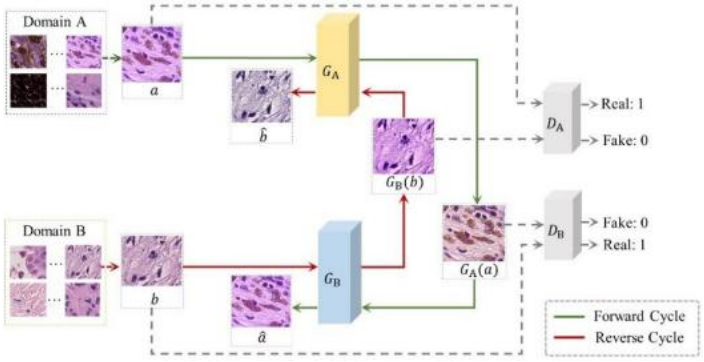

Figure 3*CycleGAN-Stain Architecture*

2.4 Deep Learning Prediction

Given the high similarity of histopathological images in terms of morphological structure and texture features, shallow convolutional neural networks have limited ability to extract complex image features, and it is difficult to reveal in-depth information about pathological images. If the network depth is increased to overcome this problem, the problem of gradient vanishing and network performance degradation will be encountered. Therefore, this study adopts the ResNet-152 architecture (Figure 4a) proposed by He et al. [to build a DL prediction module. Compared with traditional convolutional neural networks, the main feature of ResNet-152 is the introduction of residual units (Figure 4b), which are composed of convolution (Conv), batch normalization (BN), and ReLU activation functions. By adding identity mapping, the residual mapping function $F(x) = H(x) - x$ can be implemented, which alleviates the problem of gradient vanishing and network performance degradation, accelerates the convergence speed of network training, and dramatically improves the recognition ability of deep networks. The network input is a sample image patch processed by the stain normalization method, measuring 224 × 224 × 3. First, after the convolution layer (Conv1), the input image patch is extracted conventional features to reduce the feature size, then high-level features are extracted by four residual blocks (Resblock 2–5), followed by feeding the extracted high-dimensional features into a fully connected layer (Fc6) for classification output. The classifier in Figure 4a is a SoftMax classifier, which ultimately produces the probability of three types of melanocyte lesions (malignant, atypical, and benign) for each image patch.

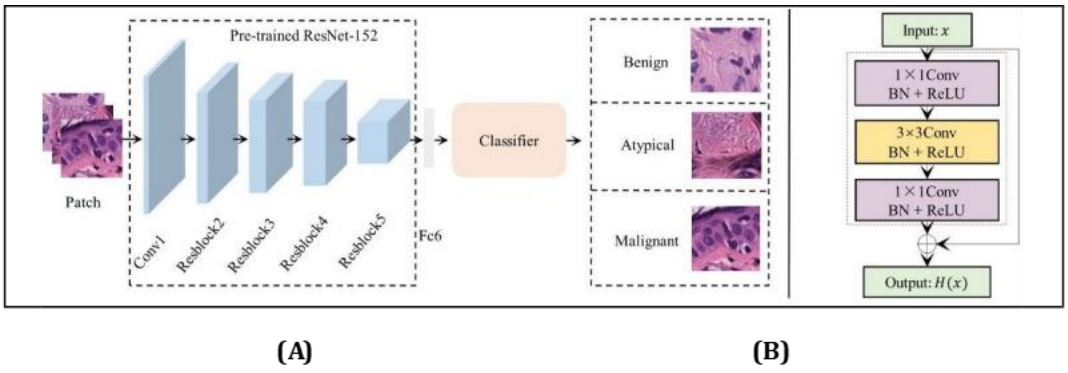

Figure 4.*DL prediction module network architecture*

2.5 Aggregation of Prediction Results

To diagnose the type of melanocytic lesion in patients, this study adopted a decision fusion strategy to combine the prediction results of all image spots from each melanocytic lesion patient. The predicted probabilities of the three lesion types from all image spots in each WSI were calculated by statistical averaging, which was considered the predicted probability of the three WSI lesion types. This was inspired by the clinical method in which pathologists tentatively classify cases with doubtful diagnoses from microscopic pathological slides as suspicious cases and then integrate the patient's clinical information for further diagnosis. In this study, we defined WSIs whose predicted probabilities of the three lesion types were lower than 0.6 as suspicious. We categorized melanocytic lesion patients whose WSIs were all suspicious as suspicious cases, which required further diagnosis by a senior pathologist in combination with review of other clinical information from the patient. Except for suspicious cases, patient WSIs were graded based on the highest malignancy grade among all WSIs, in the order of malignant > atypical > benign.

2.6 Comparison Method of Normalization of Coloring

To validate the effectiveness of the proposed staining normalization method, a comparative analysis was performed between CycleGAN-Stain and two other histopathology image staining normalization methods: a color-based method [17] and a staining-based method Furthermore, the classification performance for pathological WSI of melanocytic lesions was compared between the two methods.The color-based normalization method begins by converting the unnormalized image and the template image from the RGB color space to the orthogonal lab color space. The mean and standard deviation of the pixel intensities in the template image are calculated. A per-pixel least squares adjustment is then applied to the target image to return the image to the RGB color space.In the stain-based normalization method , by incorporating the Beer–Lambert spectral absorption law . The pathological image is converted from RGB color space to optical density space. This operation separates the stain concentration matrix A and the absorbance coefficient matrix C of the target image and the template image. Next, the stain concentration matrix A of the template image is replaced by the unnormalized image, and the inverse Beer–Lambert transform is implemented. The mathematical expression for the Beer–Lambert transform is as follows:

$$OD = -\ln\left(\frac{I}{I_0}\right) = A \cdot C, \tag{3}$$

where $I \in \mathbb{R}^{m \times n}$ denotes the transmitted light intensity of a pixel, with n denoting the number of pixels in the pathological image, and $m = 3$ denotes the three color channels (red, green, and blue). $II0$, generally assumed to be 255, denotes the incident light intensity. $A \in \mathbb{R}^{m \times r}$ denotes the stain concentration matrix; $r = 2$ denotes H and E stains; and $C \in \mathbb{R}^{r \times n}$ denotes the stain absorbance coefficient matrix.

2.7 Model Evaluation Criteria

To compare the performance of the stain normalization methods, this study uses the structural similarity metric (SSIM) and the peak signal-to-noise ratio (PSNR) for quantitative evaluation. The larger the value, the better the stain normalization method is in maintaining the consistency of the image structure. Since the difference in stain style in the image before and after stain normalization affects the SSIM and PSNR, the grayscale transformation is performed first, then the SSIM and PSNR are calculated. The calculation of SSIM and PSNR is as follows:

$$MSE = \frac{1}{mn}\sum_{i=0}^{m-1}\sum_{j=0}^{n-1}[I(i,j) - I^{norm}(i,j)]^2, \quad (4)$$

$$PSNR = 10 \cdot log_{10}\left(\frac{MAX_I^2}{MSE}\right), \quad (5)$$

$$SSIM(I, I^{norm}) = \frac{(2\mu_1\mu_2 + C_1)(\sigma_{12} + C_2)}{(\mu_1^2 + \mu_2^2 + C_1)(\sigma_1^2 + \sigma_2^2 + C_2)}, \quad (6)$$

where I denotes the unnormalized image with size $m \times l$, and I^{norm} denotes the normalized image. MAX^1_i is the maximum pixel value of image I, which is usually 255. $\mu 1$ and $\mu 2$ denote the average pixels of I and I^{norm}, respectively. $\sigma 1$ and $\sigma 2$ are the standard deviations of I and I^{norm}, respectively. $\sigma 12$ is the covariance of I and I^{norm}.$C1$ and $C2$ are constants to avoid division by zero.To evaluate the classification performance of the diagnostic model, this study uses classification accuracy (ACC) and macro F1 score for quantitative evaluation. The higher the value, the better the model's diagnostic performance. The calculation of ACC and macro F1 score is as follows:

$$Acc = \frac{TP+TN}{TP+FP+TN+FN}, \quad (7)$$

$$Recall = \frac{TP}{TP+FN}, \quad (8)$$

$$Precision = \frac{TP}{TP+FP}, \quad (9)$$

$$F1\ score = 2\frac{Recall \times Precision}{Recall + Precision}, \quad (10)$$

$$macro\ F1 = \overline{F1\ score}, \quad (11)$$

where true positives (TP) indicates the number of positive samples that are correctly classified; false positives (FP) indicates the number of negative samples that are incorrectly classified as positive; true negatives (TN) indicates the number of negative samples that are correctly classified; and false negatives (FN) indicates the number of positive samples that are incorrectly classified as negative.

3. Results and Discussion

3.1 Data Source

A total of 218 patients with malignant, 119 atypical, and 374 benign melanocytic lesions diagnosed between 2001 and 2018 were enrolled from Shanghai Jiao Tong University School of Medicine Affiliated Ninth People's Hospital (“Center 1”), Shanghai Jiao Tong University School of Medicine Affiliated Ninth People's Hospital North Branch (“Center 2”), and Shanghai First People's Hospital Baoshan Branch (“Center 3”). Hematoxylin & eosin (H&E) stained slides from all patients were obtained. All patients had a definitive diagnosis (benign, atypical, or malignant), primarily determined by a pathologist through microscopic observation of cellular structure and morphology. If the H&E diagnosis was uncertain, the patient's clinical manifestations and immunohistochemical/molecular detection results were combined for diagnosis. All H&E slides included in this study were re-evaluated by a senior pathologist with 30 years of pathological diagnosis experience in dermatological diseases.

All H&E slides were scanned with a Hamamatsu NanoZoomerS60 scanner at 40x magnification, resulting in 457 WSIs of malignant, 142 atypical, and 382 benign melanocytic lesions. All WSIs were annotated by two pathologists with eight and 15 years of experience in the pathological diagnosis of dermatological diseases. The two pathologists used the medical image processing software NDP.view2 (version 2.6.13) to annotate each lesion area, assuming the WSI lesion type was known. To address inconsistencies in the annotation results, the pathologists reached a consensus by considering the patient's clinical information (gender, age, anatomical location, etc.) and through group discussion.

The WSI of patients with melanocytic lesions in Center 1 was divided into a training set and an internal testing set using stratified random sampling with a ratio of 8:2, and the WSI of patients with melanocytic lesions in Center 2 and Center 3 was used as an external testing set (Table 1).

Table 1.*Number of patients and WSI in training and test sets*

Type of Lesion	Training Set		Internal Test Set		External Test Set	
	Patient	WSI	Patient	WSI	Patient	WSI
Benign	282	290	71	71	21	21
Atypical	88	107	23	26	8	9
Malignant	162	348	42	85	14	24
Total	532	745	136	182	43	54

3.2 Experimental Environment and Hyperparameter Settings

An intelligent pathological diagnosis model was built using the open-source Python machine learning library PyTorch and an NVIDIA GTX 2080Ti GPU. The template images (Figure 5a) for the color-based staining and stain-based staining methods were selected by pathologists based on the staining effects of pathological tissues. Through experimental analysis, the network training hyperparameter settings for the CycleGAN-Stain staining normalization method and the DL prediction module were determined; both are shown in Table 2. The DL prediction module adopts a multiclass cross-entropy loss function and initializes a ResNet-152 network with weights pre-trained on the ImageNet dataset.

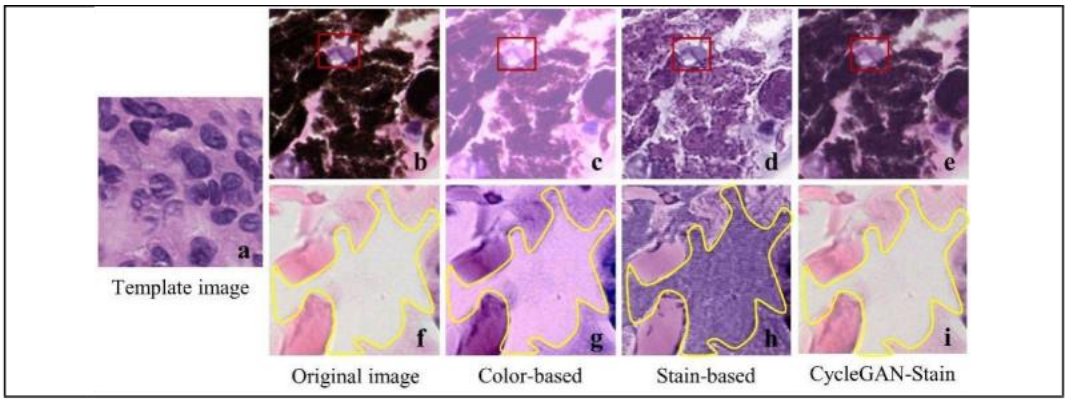

Figure 5*Pathology image staining normalization results*

Table 2 *Hyperparameter settings for training intelligent pathological diagnosis models*

Network Architecture	Optimizer	Learning Speed	Batch Size	Time
CycleGAN	Adam	0.0002	2	200
ResNet-152	Adam	0.00001	16	400

3.3 Comparison of Stain Normalization Performance and Disease Diagnosis

This study randomly extracted 300 unnormalized image patches from the dataset and processed them using three colorization normalization methods. Next, the average SSIM and PSNR values were calculated for the 300 image patch pairs before and after colorization normalization, as shown in Table 3.

Table 3 *Image quality evaluation after blemish normalization*

Stain Normalization Method	Color Based Method	Stain-Based Method	CycleGAN Coloring Method
SSIM	0.902	0.880	**0.963**
PSNR (dB)	20,024	22,821	**32,622**

To visually demonstrate the staining normalization capabilities of the various methods, two pathological image patches of melanocytic lesions and their staining normalization results using the three methods were randomly selected, as shown in Figure 5.

The ACC and macro F1 scores of the intelligent pathological diagnosis model on the unnormalized dataset and the dataset processed by the three staining normalization methods are shown in Table 4.

Table 4 *Comparison of intelligent pathological diagnosis results*

Stain Normalization Method	Internal Test Set		External Test Set	
	ACC	FI Macro	ACC	FI Macro
Not normalized	93.38%	0.933	76.74%	0.843
Color Based Method	91.18%	0.889	88.37%	0.901
Stain-Based Method	92.65%	0.902	88.37%	0.859
CycleGAN Coloring Method	94.12%	0.938	90.70%	0.949

The results in Table 3 demonstrate that the CycleGAN-Stain method excels in maintaining image structural consistency. As shown in Figure 5b, the tissue within the red rectangular region has different staining properties from the surrounding tissue due to its different types, resulting in varying staining results. The CycleGAN-Stain method effectively preserves the color differences caused by tissue variation (Figure 5e), while the color-based and staining-based methods lose this important discriminatory staining information, resulting in over-normalization (Figure 5c and Figure 5d). Figures 5f, 5g, and 5h together illustrate that the color-based and staining-based methods produce normalization artifacts (in the yellow regions) that inappropriately convert non-diagnostic background regions into diagnostic tissue regions. This directly leads to erroneous diagnostic evaluations. Overall, CycleGAN-Stain outperforms the color-based and staining-based methods in maintaining histological structural consistency and suppressing such artifacts. Furthermore, CycleGAN-Stain performs style mapping between image domains, rather than

between images, which maximally preserves all structural information of pathological tissues, thus laying the foundation for building an intelligent pathological diagnosis model with strong generalization performance. As shown in Table 4, the intelligent pathological diagnosis model using CycleGAN-Stain has the strongest diagnostic performance, with an ACC exceeding 90.00% on the external test set. It is worth noting that the ResNet-152 network used in this study is a commonly used architecture for medical image processing tasks, with solid feature extraction capabilities. This network can fully utilize morphological features that have low discrimination and are invisible to the naked eye when classifying melanocytic lesions, thus providing strong support for precise diagnosis of melanocytic lesions. The decision fusion strategy used in this study allows the input to be pathological WSI data of melanocytic lesion patients and the output to be lesion types of melanocytic lesion patients, thus achieving an end-to-end intelligent pathological diagnosis of melanocytic lesions.However, a limitation of this study is that the external test set in this study consisted of a relatively small dataset, and the intelligent diagnostic model was only trained on patient histological slide data. Future studies should aim to collect more data on melanocytic lesion patients from various medical centers to validate the diagnostic performance of our intelligent model and explore methods for integrating clinical data into the model construction to improve diagnostic intelligence and practical applications.

4. Conclusions

ConclusionThis study proposes a DL-based intelligent pathological diagnosis method for classifying melanocytic lesions. Our CycleGAN-Stain method for normalizing melanocytic pathological WSI staining eliminates differences in staining styles between different WSIs. Then, the melanocytic lesion classification network we built based on the ResNet-152 architecture and decision fusion strategy we used to aggregate melanocytic lesion types from all WSIs for each patient helped to obtain the patient's final diagnosis. We anticipate that this approach will improve the diagnostic efficiency of melanocytic lesions.

References

Amrutkar, S., Sagare, P., Bhegade, P., Waykar, P., Bhalerao, M., & Kamble, M. P. (2008). International Journal of Innovative Research in Science Engineering and Technology (IJIRSET) Drip Irrigation. 9001(3), 2411. https://doi.org/10.15680/IJIRSET.2025.1403164

Ashokan, A. (2024). Comparative Analysis of CycleGAN and StyleGAN in Unpaired Image-to-Image Translation and High-Quality Image Synthesis. July, 274–278. www.irjet.net

Bian, Q., Zhang, J., & Serrano, E. A. (2025). Intelligent Pathological Diagnosis of Melanocytic Lesions Using Deep Learning. Journal of Soft Computing and Data Mining, 6(1), 86–94. https://doi.org/10.30880/jscdm.2025.06.01.006

Calista, TR, Majid, NWA, & Andrian, R. (2023). Implementation of Image Processing and Histogram of Oriented Gradient to Detect Parking Slots in a Supermarket. Journal of Information Systems and Technology (JustIN), 11(3), 453. https://doi.org/10.26418/justin.v11i3.55412

Icanervilia, AV, Choridah, L., Van Asselt, ADI, Vervoort, JPM, Postma, MJ, Rengganis, AA, & Kardinah, K. (2023). Early Detection of Breast Cancer in Indonesia: Barriers Identified in a Qualitative Study. Asian Pacific Journal of Cancer Prevention, 24(8), 2749–2755. https://doi.org/10.31557/APJCP.2023.24.8.2749

Jay, F., Renou, J.-P., Voinnet, O., & Navarro, L. (2017). Unpaired Image-to-Image Translation using Cycle-Consistent Adversarial Networks Jun-Yan. Proceedings of the IEEE International Conference on Computer Vision, 183–202. http://link.springer.com/10.1007/978-1-60327-005-2_13

Lorandi, M., Mohamed, M.A., & Mcguinness, K. (nd). Adapting the CycleGAN Architecture for Text Style Transfer.

Mabu, S., Miyake, M., Kuremoto, T., & Kido, S. (2021). Semi-supervised CycleGAN for domain transformation of chest CT images and its application to opacity classification of diffuse lung diseases. International Journal of Computer Assisted Radiology and Surgery, 16(11), 1925–1935. https://doi.org/10.1007/s11548-021-02490-2

Nasir, J., & Azhar Ramli, A. (nd). Design of Door Security System Based on Face Recognition with Arduino.

Nasir, J., Ramli, AA, & Kasim, S. (2017). An initial framework of hybrid evolutionary algorithm (EA) with Multiple Criteria Decision Making (MCDM): Plant forecasting scenario. 2017 International Conference on Sustainable Information Engineering and Technology (SIET), 13(6), 144–149. https://doi.org/10.1109/SIET.2017.8304125

Nunez, N. A., & Barrios, M. (2023). Do Technology Startups Replicate Internationalization Patterns From Big Companies? Evidence From Latin America. TEM Journal, 12(4), 2350–2360. https://doi.org/10.18421/TEM124-47

Priswanto, B., & Santoso, H. (2022). CycleGAN and SRGAN to Enrich the Dataset. SinkrOn, 7(2), 495–503. https://doi.org/10.33395/sinkron.v7i2.11384

Raihan Taufiq, MF, & Rahadianti, L. (2025). CycleGAN for day-to-night image translation: a comparative study. IAES International Journal of Artificial Intelligence, 14(3), 2347–2357. https://doi.org/10.11591/ijai.v14.i3.pp2347-2357

Rani, S., Mishra, A.K., Kataria, A., Mallik, S., & Qin, H. (2023). Machine learning-based optimal crop selection system in smart agriculture. Scientific Reports, 13(1), 1–11. https://doi.org/10.1038/s41598-023-42356-y

Riesmiyatiningdyah, R., Murtiyani, N., Ridi, KW, Province, EJ, Husada, D., Academy, N., & Province, EJ (2022). GROUP ACTIVITY THERAPY TO IMPROVE COGNITIVE FUNCTION OF THE ELDERLY BY GUESSING THE. 4(2), 40–44.

Smoczek, J. (2013). Evolutionary optimization of interval mathematics-based design of a TSK fuzzy controller for anti-sway crane control. International Journal of Applied Mathematics and Computer Science, 23(4), 749–759. https://doi.org/10.2478/amcs-2013-0056

Sun, L., Shen, D., & Feng, H. (2024). Theoretical Insights into CycleGAN: Analyzing Approximation and Estimation Errors in Unpaired Data Generation. http://arxiv.org/abs/2407.11678

Temani, A., & Feng, Y. (2020). Pr ep rin tn ot pe er r iew Pr rin tn ot pe ed.

Wang, H., Czerminski, R., & Jamieson, A.C. (2021). Neural Networks and Deep Learning. The Machine Age of Customer Insight, 91–101. https://doi.org/10.1108/978-1-83909-694-520211010

Yang, B., Chang, Y., Liang, Y., Wang, Z., Pei, X., Xu, X. G., & Qiu, J. (2022). A Comparison Study Between CNN-Based Deformed Planning CT and CycleGAN-Based Synthetic CT Methods for Improving iCBCT Image Quality. Frontiers in Oncology, 12(March), 1159770. https://doi.org/10.3389/fonc.2022.896795